INORGANIC CHEMISTRY
FRONTIERS

RESEARCH ARTICLE

View Article Online
View Journal | View Issue

Cite this: *Inorg. Chem. Front.*, 2022, **9**, 859

A fluorescent zirconium organic framework displaying rapid and nanomolar level detection of Hg(II) and nitroantibiotics†

Subhrajyoti Ghosh,[a] Felix Steinke,[b] Abhijeet Rana[a] and Shyam Biswas *[a]

The solvothermal reaction of $ZrCl_4$ with a benzo[1,2-*b*:4,5-*b*']dithiophene-2,6-dicarboxylic acid (**L1**) linker molecule in the presence of a trifluoro acetic acid modulator afforded a UiO-66 type of metal organic framework (MOF) (**IITG-5**, IITG = Indian Institute of Technology, Guwahati). The synthesized MOF material was characterized in detail with the help of PXRD, FE-SEM, FT-IR, EDX and elemental analyses. The material showed high thermal stability up to 390 °C in air atmosphere. This porous material (surface area = 1228 m^2 g^{-1}) also displayed significant chemical stability in various solvents. The thermally activated compound (**IITG-5a**) exhibited excellent detectability towards Hg^{2+} in aqueous medium and various nitro-antibiotics (nitrofurazone and nitrofurantoin) in MeOH. Besides the fast response (1 min for all analytes), very low limits of detection (LODs) were observed for the sensing of all the targeted analytes (LOD for Hg^{2+}, nitrofurazone and nitrofurantoin were 5, 156.7 and 96.3 nM, respectively). A paper strip-based sensing technique was developed for all the three analytes. Interestingly, for the sensing of all the above-mentioned analytes, **IITG-5a** featured excellent reusability of up to five consecutive cycles without loss of its sensing efficiency. Mechanisms for all the sensing actvities were elaborately explored by means of DFT calculations and analytical methods.

Received 18th September 2021,
Accepted 8th January 2022

DOI: 10.1039/d1qi01190a

rsc.li/frontiers-inorganic

Introduction

Mercury (Hg) is a highly toxic, non-biodegradable and soft heavy metal.[1] In the year 1956, Japan's minamata disease already displayed the horrible toxic effect of Hg.[2] In the environment, Hg is mainly present in its inorganic salt form. However, the inorganic form of Hg^{2+} can easily be converted into its more toxic form methylmercury (CH_3Hg^+) by fish and microorganisms.[3] Due to the soft and lipophilic nature of CH_3Hg^+, it can be easily absorbed by the human body.[3] This toxic heavy metal mainly enters into the human body *via* aquatic organisms. Even a trace amount of mercury can easily bind with soft sulphur-containing amino acid molecules of living organisms and collapse the immune and central nervous systems.[4,5] Absorption of higher concentrations of Hg can cause cancer, heart troubles, respiratory failure, motion disorder, temporary blindness, kidney failure, intelligence loss, nephrotic syndrome, *etc.*[6] In spite of the large number of toxic effects of Hg, the on-going development of various industries, numerous natural phenomena like volcanic eruption and human activities (*e.g.* burning of coal, waste incineration, and combustion of fossil fuels) increase Hg pollution.[7] Therefore, environmental pollution caused by Hg has become a global issue of high concern, which must be resolved urgently.

In the modern day, different types of pharmaceutical antibiotics are being used all over the world for the purpose of human therapy and the farming industry.[8] In the year 1928, the first antibiotic penicillin was discovered.[9] Thereafter, in the last 90 years, a variety of antibiotics have been developed to get rid of different bacterial diseases.[10,11] However, the excessive use and arbitrary disposal of the poorly metabolized antibiotics created lot of problems for the environment as well as for living beings.[12,13] Long-term intake of antibiotics may give rise to the development of antibiotic resistant genes in living organisms, which have serious effects on the ecosystem.[13,14] The residues of pharmaceutical antibiotics and their various transformed products may cause different adverse effects like chronic and acute toxicity and microorganism antibiotic resistance.[15] Nitrofurazone (NFZ) and nitrofur-

[a]*Department of Chemistry, Indian Institute of Technology Guwahati, Guwahati, 781039 Assam, India*
[b]*Institut für Anorganische Chemie, Christian-Albrechts-Universität, Max-Eyth-Strasse 2, 24118 Kiel, Germany*

† Electronic supplementary information (ESI) available: Linker synthesis details, ^1H NMR, mass, ^{13}C NMR of free linker, FT-IR spectra of MOF and free linker, TGA curves, FE-SEM images, BET isotherms, porosity distribution curve, fluorescence spectra, TRPL plots, UV-Vis spectra and recyclability plot. See DOI: 10.1039/d1qi01190a

antoin (NFT) are two very common antibiotics, which are mainly used for the remedy of skin infections, and urinary tract and kidney infections, respectively.[16,17] Exposure to these antibiotics for a long time may cause several side effects such as nausea, vomiting, headache, loss of appetite and dizziness.[18,19] Thereafter, it is necessary to develop a suitable method to prevent the environmental pollutions caused by these antibiotics.

One of the most common ways to prevent the environment and living beings from the toxic effects of heavy metal ions (Hg) and various antibiotics (NFZ and NFT) is to know their presence in the environmental samples (soil and water). Fluorometric method is one of the most user-friendly, easily accessible, rapidly responsive, low-cost and reliable methods of sensing.[20] Such features have made the fluorescence-based method of sensing more popular in scientific community than other conventional techniques of sensing such as HPLC, capillary electrophoresis, LC-MS, atomic emission and absorption spectroscopy.[21] The choice of appropriate sensor molecules (fluorophores) can permit the easy sensing of the targeted analytes.

Fluorescent MOFs contain ligands such as fluorophores, which are able to sense various metal ions, anions, biologically signalling molecules, various toxic gas molecules, antibiotics, *etc.*, in the past few years.[22–25] Rapid development of various MOF-based sensors took place in recent times because of their high physicochemical stability, porous nature and tuneable nature of functional groups (as required) even after their synthesis.[24,26] Wide choice of solvent molecules for the sensing purpose and stability in a H_2O medium have made MOF materials suitable sensing probes for various analytes.[27]

Various sulphur-containing organic linker molecules and MOFs are reported in the literature, which were used for the sensing of Hg^{2+}. For the sensing of various nitro-group-containing antibiotics, an electron-rich probe can be used.[26,27] The interaction between the soft sulphur atom with soft Hg^{2+} ions and intermolecular energy transfer is the probable reason behind the sensing of Hg^{2+} ions and nitro-group-containing antibiotics in most of the reported probes.[28–30]

Thereby, we strategically synthesized a Zr-based UiO-66 MOF material using benzo[1,2-*b*:4,5-*b*′]dithiophene-2,6-dicarboxylic acid linker (**L1**). Our aim was to utilise such a linker for the sensing of Hg^{2+} and various nitro-group-containing antibiotics. In reality, the thermally activated MOF material displayed outstanding selectivity towards the sensing of Hg^{2+} and nitro-group-containing antibiotics (NFZ and NFT) (Scheme 1). Rapid responses were observed in both the cases of sensing (for Hg^{2+} = 1 min; for NFZ = 1 min and for NFT = 1 min). In addition to fast and selective responses, this MOF material also exhibited extraordinarily low LODs for all the targeted analytes (LOD is 5 nM for Hg^{2+}, 156.7 nM for NFZ and 96.3 nM for NFT). Together with the solvent phase, this newly synthesized MOF material can also sense the targeted analytes in a paper strip coated with MOFs.

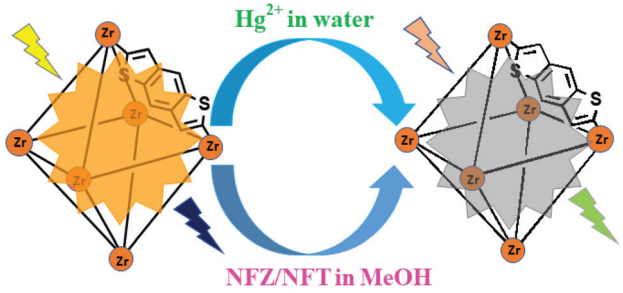

Scheme 1 Fluorogenic switch-off sensing of Hg^{2+} and NFT/NFZ by **IITG-5a**.

Experimental section

Synthesis of $[Zr_6O_4(OH)_4(C_{12}H_4S_2)_{4.9}]\cdot 4H_2O\cdot 4DMF$ (IITG-5)

A mixture of a benzo[1,2-*b*:4,5-*b*′]dithiophene-2,6-dicarboxylic acid linker molecule (20 mg, 0.07 mmol), a $ZrCl_4$ metal salt (17 mg, 0.07 mmol), trifluoroacetic acid (166 μL, 2.1 mmol) and 3 mL DMF was sonicated for 30 min after pouring all the components into a Pyrex tube. Here, the linker molecule, $ZrCl_4$ and trifluoroacetic acid modulator were taken in a molar ratio of 1 : 1 : 30. After complete dissolution of all the components by sonication, the mixture was positioned on a pre-heated heating block at 150 °C for 1 day. After 1 day, a yellow colour solid precipitate (**IITG-5**) was collected *via* filtration. The obtained solid was washed with acetone (3 × 2 mL) and placed in an 80 °C air oven for 6 h. Yield: 25 mg (0.01 mmol, 77%) related to Zr salt. Anal. calcd for $C_{70.8}H_{59.6}N_4O_{16}S_{9.8}Zr_6$ (2075 g mol^{-1}): C, 40.94; H, 2.87; N, 2.70. Found C, 40.59; H, 2.72; N, 2.56%. FT-IR (cm^{-1}): 3387 (br), 2846 (w), 2550 (w), 1654 (s), 1542 (vs), 1445 (s), 1402 (vs), 1358 (s), 1310 (s), 1253 (w), 1162 (s), 1075 (m), 886 (m), 773 (s), 660 (s), 602 (m), 442 (s).

Activation of compound IITG-5

In the as-prepared compound (**IITG-5**), some DMF molecules were encapsulated within the pore. To remove the DMF molecules, at first 50 mg of **IITG-5** was stirred in 100 mL of methanol (MeOH) for 1 day. Then, the recovered material was collected by filtration and completely dried in an oven at 60 °C for 1 day. Finally, the low boiling MeOH solvents (encapsulated within the pore of **IITG-5** during solvent exchange) were removed by heating the compound in a 100 °C oil-bath for 1 day under vacuum. Thus, we obtained the thermally activated compound **IITG-5a**.

Rietveld refinement

At first, a starting model for the Rietveld refinement based on the UiO-66 structure[31] was built using Materials Studio[32] and geometrically optimized applying force-field calculations. For the refinement using Topas Academics,[33] the bond lengths of the Zr–O-bonds of the hexanuclear cluster were restrained. For the C–C-, C–S- and C–O-bonds of the linker, a set of distance and angle restraints were used. Since the linker is placed on a mirror plane, the atoms S1 and C3 were refined almost on top

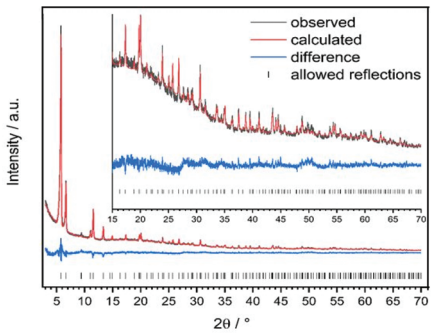

Fig. 1 Rietveld plot for the structural refinement of **IITG-5a**.

of each other, but with an occupancy of 0.5 respectively. No indication for a preferred orientation of the linker molecule was found. The final parameters obtained from the Rietveld refinement are summarized in Table S7.† The Rietveld plot is displayed in Fig. 1 and the details of bond lengths in the structure of **IITG-5** are shown in Table S1 (ESI†).

Results and discussion

Analysis of structure

At first, PXRD analysis with both **IITG-5** and **IITG-5a** was performed (Fig. S5, ESI†). The obtained PXRD data of **IITG-5** were indexed. This resulted in a cubic space group ($Fm\bar{3}m$, no. 225). By utilizing the obtained lattice parameters from refinement (Table S7†) and the crystal structure of UiO-66, a model for the structure of **IITG-5** was constructed. The modelled crystal structure of **IITG-5** was refinement *via* the Rietveld method utilizing the PXRD data of the compound. To our satisfaction, the refinement results indicated that the structure of **IITG-5** (Fig. 2) owns a similar framework structure to UiO-66.[31] Similar to pristine UiO-66 framework, **IITG-5** also has octahedral and tetrahedral structural voids. Here, all the Zr-atoms are present in a square antiprismatic coordination environment. Such similarities in both the structures imply that the incorporation of benzo[1,2-*b*:4,5-*b*′]dithiophene-2,6-dicarboxylic acid linker molecules in place of un-functionalized terephthalic acid linker molecules does not make any change in the framework structure. The activated compound (**IITG-5a**) also displayed a similar PXRD pattern to that of **IITG-5**. That means, the framework of **IITG-5** remains un-altered even after thermal activation. A homogeneous crystalline phase consisting of cubic shaped crystals of **IITG-5a** was visualized from the FE-SEM images (Fig. S6, ESI†). The presence of C, S, O and Zr atoms in the MOF was confirmed by the EDX analysis (Fig. S34, ESI†).

Infrared (IR) spectroscopy

To ensure the presence of various functional groups and the whole removal of DMF (solvent) molecules from the pore of the framework structure, we took the support of FT-IR spectroscopy (Fig. S4, ESI†). Two sharp absorption bands at 1542 and 1402 cm^{-1} were observed in case of both **IITG-5** and **IITG-5a**, which originated from the Zr-coordinated asymmetric and symmetric stretching of carboxylate groups of the linker molecules. A weak absorption band near 1654 cm^{-1} was observed for compound **IITG-5**, which denotes the carbonyl stretching vibration of DMF molecules. Such an absorption frequency was not observed in case of **IITG-5a**. This confirmed the whole removal of guest DMF molecules from the pore of the framework structure of **IITG-5**.

Thermal stability

Thermogravimetric analysis (TGA) of both **IITG-5** and **IITG-5a** was conducted to know the thermal stabilities of this newly synthesized MOF material in as-synthesized (**IITG-5**) and activated forms (**IITG-5a**). Fig. S7 (ESI†) displays that both **IITG-5** and **IITG-5a** are thermally stable up to a temperature of 390 °C in air. For the as-synthesized compound (**IITG-5**), three consecutive losses of weights took place. The first loss of weight

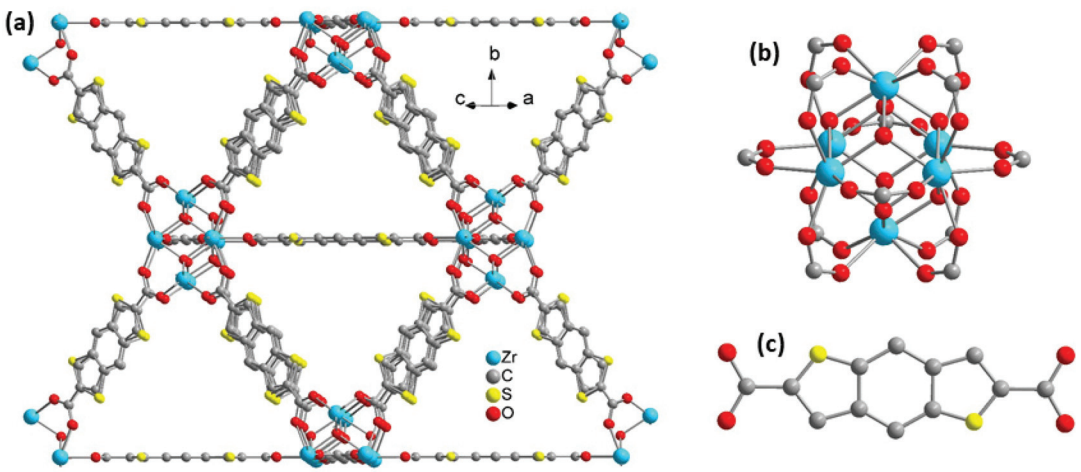

Fig. 2 Structure of the compound **IITG-5** (a), its SBU (b) and corresponding linker (c).

(2.6%) in between the temperature of 25–120 °C could be attributed to the loss of 4 H_2O molecules per formula unit (calcd.: 2.6 wt%). Escaping of 4 DMF molecules (per formula unit) from the pore of the framework is the reason behind the weight loss of 11.2% within the temperature range of 120–230 °C (calcd.: 11.3 wt%). Beyond a temperature of 390 °C, decomposition of the framework structure took place. In case of **IITG-5a**, weight loss was observed only at temperatures above 390 °C due to decomposition of the framework structure. Hence, it can be concluded that both **IITG-5** and **IITG-5a** have similar thermal stabilities to that of the other reported UiO-66 family of Zr-MOFs.[34,35]

The experimental and theoretical weight losses due to the degradation of the organic linkers were ~57% and ~71%, respectively. Such a difference between experimental and theoretical weight losses clearly indicates that there are some linker defects in the MOF structure. The weight loss owing to the degradation of the linker molecules suggests that 4.9 linker molecules are present per formula unit of the framework. This result eventually implies that 1.1 linkers are missing per formula unit of MOFs.

Chemical stability

Chemical stability of **IITG-5a** in different solvents (H_2O, MeOH, CH_2Cl_2, acetone, hexane and DMF) was investigated (Fig. S8, ESI†). For this investigation, at first, 15 mg of **IITG-5a** was stirred in 20 mL of different solvents at room temperature for 6 h. Afterwards, the material was collected by filtration and PXRD analysis was performed after drying the recovered material at 60 °C inside an oven. The unperturbed nature of the PXRD patterns confirms the stability of **IITG-5a** in various solvents. The robust nature of the material in the sensing media (H_2O and MeOH) fulfills the criteria of a smart sensor molecule. Therefore, the chemical stability of **IITG-5a** is comparable to other reported UiO-66 types of Zr-MOFs.[34,36]

N_2 sorption analysis

For the determination of surface area (BET) and pore volume of **IITG-5a**, the N_2 sorption analysis was performed at a temperature of −196 °C (Fig. S9, ESI†). The N_2 sorption study and density functional theory pore-size distribution plot (Fig. S10, ESI†) confirms the microporous nature of the framework. The obtained surface area of **IITG-5a** was 1228 $m^2\ g^{-1}$ with a pore volume of 0.6 $cm^3\ g^{-1}$ (measured at p/p_0 = 0.5). The average pore radius was 10.8 Å. Therefore, it is worthy to state that the BET surface area of **IITG-5a** is comparable to the other Zr-based UiO-66 types of materials reported in the literature.[35,37] We also conducted the BET surface area analysis after stirring the MOF material in different solvents for 6 h. The obtained BET surface areas of the recovered materials after stirring in H_2O, MeOH, CH_2Cl_2, acetone, hexane and DMF solvents were 1196, 1192, 1239, 1184, 1231 and 1170 $m^2\ g^{-1}$, respectively (Fig. S11–S16, ESI†). The obtained surface areas were similar to the surface area of the fresh MOF material (1228 $m^2\ g^{-1}$). These experiments clearly support the structural stability of the MOF in the above-mentioned solvent systems for 6 h.

Particle size determination for IITG-5a in sensing media

The particle size of **IITG-5a** was measured by a dynamic light scattering method. The average particle sizes of the MOF after three measurements were 956 nm and 994 nm for the aqueous and MeOH dispersions, respectively (Fig. S82, ESI†). The polydispersion index (0.29 and 0.35 in H_2O and MeOH, respectively) values also signified the narrow distribution of the particle size. The obtained particle sizes clearly proved that the MOF particles have a diameter in the colloidal region.

Fluorescence sensing of Hg^{2+} in water

Various small organic sensor molecules and MOF materials were reported for the sensing of Hg^{2+}. However, in most cases, the sensors suffer from poor selectivity of sensing, long response time, unsatisfactory limit of detection, lack of recyclability of the sensing probe and choice of an organic solvent as a sensing medium.[38,39] To ensure the capability of **IITG-5a** for the sensing of Hg^{2+} in the universal solvent (H_2O), at first, we conducted the fluorescence titration experiment with the aqueous suspension of **IITG-5a** (100 μL) (taken in a 3 mL cuvette containing 2900 μL of H_2O) by adding an incremental volume of 25 μL of aqueous solution (10 mM) of Hg^{2+}. Initially, **IITG-5a** displayed very high luminescence emission intensity but with the incremental addition of Hg^{2+} solution, and the emission intensity gradually decreased and finally became saturated after addition of 75 μL of 10 mM aqueous solution of Hg^{2+} (λ_{ex} = 320 nm, λ_{em} = 420 nm) (Fig. 3). Around 92% decrease in fluorescence intensity was observed after the addition of 75 μL of a 10 mM solution of Hg^{2+}.

A time-dependent luminescence study was conducted to deduce the response time of **IITG-5a** for the sensing of Hg^{2+} (Fig. 4). We know that the sensors with a lower response time are more applicable for the real-life sensing purpose. At first, 100 μL of aqueous suspension of **IITG-5a** was taken in a cuvette containing 2900 μL of water. It was followed by inclusion of 75 μL of 10 mM aqueous Hg^{2+} to that mixture, and fluorescence spectra were recorded with a regular time interval of 1 min. It was observed that the emission spectrum

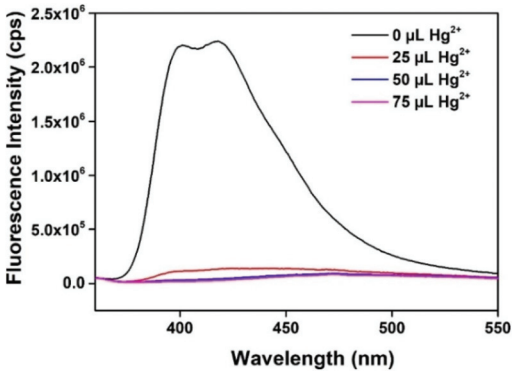

Fig. 3 Decrease in emission intensity of **IITG-5a** with the incremental addition of 10 mM aqueous solution of Hg^{2+} (from 0 μL to 75 μL) (λ_{ex} = 320 nm and λ_{em} = 420 nm).

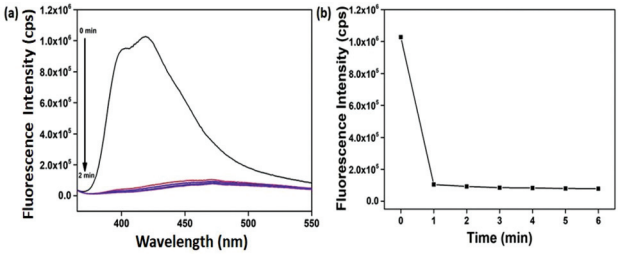

Fig. 4 (a) Switch-off in the luminescent intensity of **IITG-5a** with the increase in time after the addition of 75 μL of 10 mM Hg^{2+} solution (λ_{ex} = 320 nm, λ_{em} = 420 nm). (b) Change in luminescent emission intensity with increase in time.

rapidly became saturated after 1 min of the addition of Hg^{2+} (Fig. 4). Therefore, this probe will be highly applicable for the real-life detection of Hg^{2+} because of its very low response time (1 min).

A reliable sensor material should sense the targeted analyte only. To verify this criteria, we conducted similar sensing experiments using the other competitive metal ions (Fe^{2+}, Cu^{2+}, Al^{3+}, K^{+}, Ni^{2+}, Cd^{2+}, Na^{+}, Mn^{2+}, Cr^{3+}, Zn^{2+}, Co_2^{+}, Pb^{2+}, Pd^{2+} and Pt^{2+}) of Hg^{2+}. Fig. 5 and Fig. S19–S32 (ESI†) display that no other competitive metal ion can effectively quench the fluorescence emission intensity of **IITG-5a**. Thus, we can conclude that **IITG-5a** is highly selective to sense Hg^{2+} in H_2O.

In actual situation, more than one competitive analyte can be present together. A smart sensor should have the quality to sense the targeted analyte even in the presence of other competitive analytes. To corroborate this phenomenon, at first, we treated the aqueous suspension of **IITG-5a** with 75 μL of a 10 mM solution of other competitive analytes. Thereafter, the suspensions were further treated with 75 μL of 10 mM aqueous solution of Hg^{2+}. From Fig. S19–S32 (ESI†) and Fig. S33 (ESI†) it can be evidenced that the fluorescence intensities of **IITG-5a** were not effectively quenched in the presence of other competitive analytes. However, a rapid decrease in fluorescence intensities was observed after the addition of

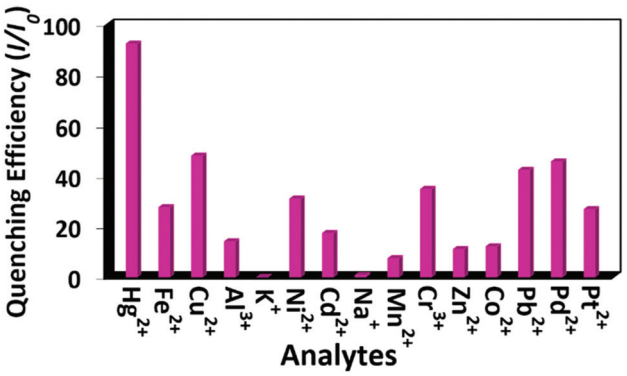

Fig. 5 Turn-off in emission intensity of **IITG-5a** after the inclusion (75 μL) of 10 mM Hg^{2+} solution and 75 μL (10 mM) solutions of competitor metal ions (λ_{ex} = 320 nm, λ_{em} = 420 nm).

Hg^{2+} solution. This proved the selective nature of **IITG-5a** even in the presence of other competitive analytes.

The Stern–Volmer (S–V) plot for different concentrations of various analytes provides us valuable information of the nature of quenching. Here, sensing of Hg^{2+} takes place *via* a quenching pathway. Therefore, it is obvious to draw a S–V plot to know the mechanism behind the quenching of fluorescence intensity (Fig. S34, ESI†). Here, the K_{sv} value (K_{sv} = S–V quenching constant) was calculated using the following mathematical equation: $I_0/I = K_{sv}[Q] + 1$.

In the equation, I_0 and I denote the intensities of **IITG-5a** in the absence and presence of different analytes, respectively. [Q] represents the concentrations (in molar) of different analytes. The obtained value of K_{sv} for the sensing of Hg^{2+} was 3.54×10^5 M^{-1} (Fig. S35, ESI†), which is much higher than that of most of the other reported MOF-based sensors of Hg^{2+}.[40,41]

The limit of detection value denotes the quality of a sensing probe. To obtain the LOD value for the sensing of Hg^{2+}, at first, the standard deviation (σ) of the luminescence intensities of the suspension of **IITG-5a** (in absence of any analyte) was calculated. Afterwards, a series of fluorometric titration experiments were carried out after gradually diluting the concentration of Hg^{2+}. A straight line with a negative slope (k) was obtained after plotting the concentrations against the fluorescence emission intensities (Fig. S36, ESI†). Here, the slope k = 2184.64, which corresponds to the equation $y = -2184.64x + 1.12 \times 10^6$ and R^2 = 0.99299 (x axis represents the concentration of the analytes and y axis the obtained fluorescence intensity of **IITG-5a** after the addition of analytes). The σ value was calculated using the formula $\sigma = \sqrt{\frac{\sum (x_i - \mu)^2}{N}}$, where Σ_i = intensity maxima of each suspension of **IITG-5a** (in absence of any analyte), μ = mean of the maxima of all the intensities, and N = total number of measurement. Finally, the LOD value was calculated using the formula $3\sigma/k$. Here, the obtained LOD value (5 nM) is lower than that of most of the reported MOF-based chemosensors of Hg^{2+} (Table S5, ESI†).

Recyclability tests up to five cycles were conducted using the probe **IITG-5a**. The MOF material was recovered after each cycle by centrifugation. Then, the material was filtered, washed with H_2O for the complete removal of the previously absorbed Hg^{2+} and dried. For the use of **IITG-5a** for the next cycle of sensing, the material was stirred in MeOH for 4 h and dried at 100 °C for 12 h. Fig. S37 (ESI†) displays that the material can sense Hg^{2+} with almost equal efficiency up to five cycles. High reusability with equal efficiency ensures that the probe is highly applicable for the real-life sensing purpose.

Mechanistic investigation for Hg^{2+} sensing

Recyclability performance up to five cycles (Fig. S37, ESI†) and the integrity of the framework structure of **IITG-5a** after Hg^{2+} sensing (Fig. S39, ESI†) ensure that the sensing mechanism is not reaction-based. Many sulphur-containing sensor molecules of Hg^{2+} are available in the literature, where the interaction

between the soft sulphur (S) atoms with the soft Hg^{2+} was the reason behind the quenching of fluorescence emission intensities of the sensors.[39] We also expected here that the interaction between the sulphur atoms of the thiophene rings (present in the linker molecule) and Hg^{2+} may be the reason behind the quenching process.

To explore the actual reason of quenching, we have performed the luminescence lifetime measurements (Fig. S38 and Table S2, ESI†). Insignificant change in fluorescence lifetime (2.08 and 2.07 ns) before and after addition of Hg^{2+} confirms the static nature of quenching process.[42] Static nature of quenching ruled out the possibility of resonance energy transfer from **IITG-5a** to Hg^{2+}. Therefore, the coordinative interaction between soft sulphur atoms of **IITG-5a** and Hg^{2+} ($S\cdots Hg^{2+}$ interaction)[43] may be the reason behind the quenching process. This kind of interaction was reported for many of the sensing/absorption processes of Hg^{2+} in the literature.[28,44] Furthermore, UV-Vis, EDX and XPS analysis were performed to validate the probable interaction between the S atoms (of the linker) and Hg^{2+}. EDX analysis of the recovered material obtained after sensing displayed the presence of Hg^{2+} (3.1 wt%) (Fig. S40, ESI†). This implies that some complexation took place between Hg^{2+} and S atoms of the linker molecule. However, the retention of the PXRD profile verified that the interactions between Hg^{2+} and the S atoms of the thiophene rings are not sufficiently strong to break down the crystalline nature of **IITG-5a** (Fig. S39, ESI†). Furthermore, the possible interaction between soft S atoms of **IITG-5a** and Hg^{2+} was examined by UV-Vis spectroscopy (Fig. S41, ESI†). Before the addition of Hg^{2+}, **IITG-5a** displayed absorption peaks at 374 and 255 nm and a shoulder peak at 362 nm. However, after the inclusion of Hg^{2+}, the peak at 374 nm vanished and a new absorption peak appeared at 344 nm along with two small peaks at 381 and 403 nm. The peak at 255 nm remained at the same position. These changes in the UV-Vis spectra strongly support the interaction between the soft S atoms and Hg^{2+}.[45,46] To confirm the specific interaction between S and Hg^{2+}, we performed XPS analysis. The XPS spectra of **IITG-5a** before and after the treatment of Hg^{2+} were analysed (Fig. S42–S46, ESI†). The XPS signature of the 4f orbital of Hg^{2+} showed sharp peaks at 101.38 and 105.41 eV. This confirmed the presence of Hg^{2+} in the recovered material obtained after the sensing event. Furthermore, the XPS spectra of the fresh and Hg^{2+}-treated **IITG-5a** for Zr 3d, O 1s and C 1s orbitals were similar. However, an obvious change in the XPS spectrum of the S 2p orbital of the fresh and used **IITG-5a** confirmed the interaction between the S atoms of thiophene rings and Hg^{2+}. The peaks at 163.82, 164.88, 168.78 and 169.91 eV for fresh sample correspond to the 2p orbital of S atoms, which were shifted to the lower energy region (163.15, 164.22, 168.07 and 169.22 eV) after the treatment of Hg^{2+}. All the above-mentioned experimental results strongly support that the coordinative interactions between the S atoms of **IITG-5a** and Hg^{2+} were the reasons behind the fluorescence quenching of **IITG-5a**.

We conducted a control luminescence experiment to explore the mechanism underlying Hg^{2+} sensing using benzo[1.2-*b*:4,5-*b*′]difuran-2,6-dicarboxylic acid (**L2**) and benzo[1,2-*b*:4,5-*b*′]dithiophene-2,6-dicarboxylic acid (**L1**) linker molecules. In case of **L1** linkers, rapid and significant quenching in emission maxima was observed after the addition of 75 μL of 10 mM aqueous solution of Hg^{2+} to the aqueous solution of **L1** (100 μL). However, in case of **L2** linkers, no such decrease in emission response was observed (Fig. S47, ESI†). This observation clearly supports the coordinative interaction between soft sulphur atoms of the **L1** linker and Hg^{2+} ($S\cdots Hg^{2+}$ interaction) and such interaction results in the fluorescence quenching of **L1** linkers or **IITG-5a** MOFs.

Fluorescence sensing of antibiotics (NFZ and NFT) in MeOH

NFZ and NFT are two crucial antibiotics, which are mainly used to cure the skin infections and for the remedy of urinary tract infections, respectively.[12] Consumption of these antibiotics for a long time may cause several side effects such as nausea, vomiting, headache, loss of appetite and dizziness.[18] Overuse and arbitrary disposal of these non-biodegradable antibiotics cause environmental pollution. Several sensors and absorbent materials were developed for the detection or removal of these toxic antibiotics from the environment (Table S6, ESI†). However, for most of the cases, they fail to fulfil the expectations. Poor selectivity, long response time, lack of recyclability and insufficient stability are the major drawbacks of most of the reported sensing probes of antibiotics. In most of the reported sensors of antibiotics, the transfer of energy from highly electron-rich probes to electron-deficient antibiotics is the reason behind the sensing.[30,47] Strong fluorescence intensity of **IITG-5a** in MeOH motivated us for the sensing of antibiotics in this solvent. To verify the efficiency of **IITG-5a** for the sensing of antibiotics, first, we measured the emission intensity of **IITG-5a** (100 μL MOF in 2900 μL MeOH) after exciting the MOF suspension at 370 nm. Strong emission intensity with an emission maximum at 442 nm was observed before the addition of NFZ and NFT antibiotic solutions (Fig. S18, ESI†). However, the emission intensities of **IITG-5a** gradually decreased after each incremental accumulation of 10 mM of NFZ and NFT antibiotic solutions. The diminution of emission intensities became saturated after the addition of 100 μL of 10 mM methanolic solution of NFZ and NFT antibiotics (Fig. 6).

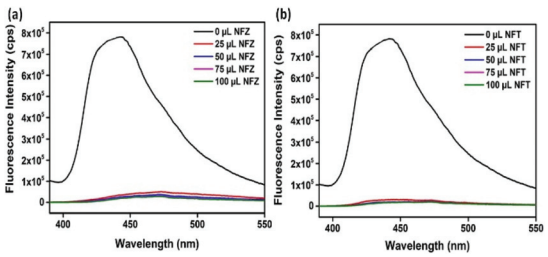

Fig. 6 Quenching in the luminescence intensity of IITG-5a with the gradual addition of 10 mM aqueous solution of NFZ (a) and NFT (b) (from 0 μL to 100 μL) (λ_{ex} = 370 nm and λ_{em} = 442 nm).

Detection time for these antibiotics by the probe was measured after addition of 100 μL of methanolic solution of NFZ and NFT antibiotics into a cuvette filled with the mixture of 100 μL MOF in 2900 μL MeOH. The reduction in fluorescence intensity became saturated after 1 min of the addition of NFZ and NFT antibiotics (Fig. 7).

The selective sensing efficiency was verified after the addition of 100 μL of 10 mM of antibiotic solutions to the suspension of 100 μL of MOF in 2900 μL MeOH. From Fig. 8 and Fig. S48–S56 (ESI†), it can be concluded that other antibiotics (except NFZ) did not effectively quench the fluorescence intensity of **IITG-5a**. Analogous experiments using 100 μL of 10 mM methanolic solution of antibiotics were performed in case of NFT. Similar results were also obtained in case of NFT (Fig. S57–S65, ESI†). All these results imply that the MOF is highly selective for the sensing of NFZ and NFT.

The selectivity of luminescence response of **IITG-5a** towards NFZ and NFT even in the presence of other competitive analytes (metronidazole (MTZ), chloramphenicol (CHL), ofloxacin (OFX), ciprofloxacin (CIP), tetracycline (TET), dimetridazole (DMZ), sulfamethazine (SMZ), ronidazole (RNZ) and sulfadiazine (SDZ)) were also verified. For this study, at first, the MOF material was treated with 100 μL of other competitive antibiotics. After that, the material was further treated with 100 μL (10 mM) MeOH solution of NFZ (identical experiments were also carried out in case of NFT antibiotic after taking 100 μL of 10 mM of NFT solution). From Fig. S66, Fig. S48–S56 and Fig. S57–S65 (ESI†), it is clear that NFT and NFZ can quench the emission intensity of **IITG-5a** with equal efficiency even in the presence of its other congeners. Therefore, we can deduce that **IITG-5a** is highly suitable for the selective sensing of NFZ and NFT in MeOH.

To realize the actual mechanism behind the quenching of fluorescence intensity in the presence of NFZ and NFT, we analysed the S–V plots (Fig. S67 and Fig. S68–S69, ESI†). The K_{sv} values were determined using the following formula: $I_0/I = K_{sv}[Q] + 1$.

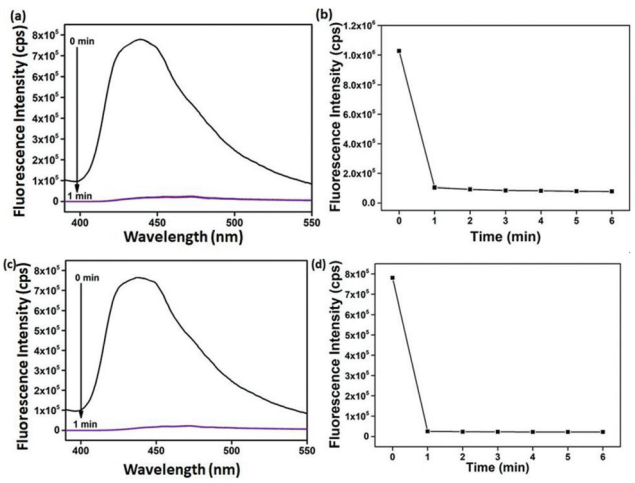

Fig. 7 Switch-off in the luminescence intensity of **IITG-5a** with respect to time after the inclusion of 100 μL of 10 mM (a) NFZ and (c) NFT solutions in MeOH. Variation in the fluorescence intensity with time for (b) NFZ and (d) NFT (λ_{ex} = 370 nm, λ_{em} = 442 nm).

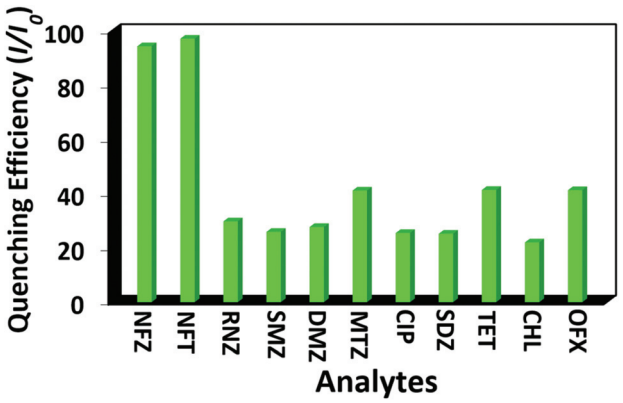

Fig. 8 Switch-off in the luminescence intensity of **IITG-5a** after the inclusion (100 μL) of 10 mM of NFZ and NFT solutions and 100 μL of 10 mM solutions (in MeOH) of other competitor antibiotics (λ_{ex} = 370 nm, λ_{em} = 442 nm).

The K_{sv} values of 1.42 × 10^5 M^{-1} and 4.3 × 10^5 M^{-1} (Fig. S68–S69, ESI†) for NFZ and NFT are more superior than most of the other reported chemosensors of nitro-antibiotics.[30,48,49] Initially, at lower concentrations of nitro-antibiotics, the S–V plots were linear in nature. However, at higher concentrations of nitro-antibiotics, they deviate from their linearity. Thereby, the energy transfer process or self-absorption may be the reason behind these quenching processes.

Similar to Hg^{2+} sensing, here also the LOD values for the detection of NFZ and NFT were calculated (Fig. S70 and S71, ESI†) using the 3σ/k rule. The final obtained values of LODs are 156.7 nM and 96.3 nM for NFZ and NFT, respectively. The obtained LOD values are much lower than most of the reported chemosensors of NFZ and NFT (Table S6, ESI†).

Reusability performance for the sensing of NFZ and NFT up to five cycles was explored (Fig. S72 and S73, ESI†). Similar experimental procedures as applied in case of Hg^{2+} sensing were followed. It is worth to note that the material is highly recyclable of the sensing of the selected nitro-antibiotics. High recyclable performance without any loss of its sensing efficiency increases its practical application possibilities.

Mechanistic investigation for NFZ and NFT sensing

Reusability of **IITG-5a** for the sensing of NFZ and NFT up to five conjugative cycles (Fig. S72 and S73, ESI†) and retention of the PXRD profile of **IITG-5a** after sensing (Fig. S39, ESI†) confirmed that the mechanism behind quenching is not reaction based. There are some basic phenomena such as collision between molecules, ground-state complexation, energy transfer process, inner filter effect (IFE) and excited-state reaction, which are reported in the literature as reasons behind quenching processes.[50] All the above-mentioned processes can be classified into two different types of quenching processes.

These are static and dynamic quenching processes. Diffusion of quencher molecules to the excited state of the fluorophore and collision between the fluorophore and the quencher molecules are the main reasons behind the dynamic quenching. However, close association between fluorophore and the quencher molecules may result in static quenching.[43]

A time-resolved fluorescence study can corroborate the nature of quenching. If the fluorescence lifetime of the excited-state fluorophore remains constant even after addition of quencher molecules, the process is static quenching. However, if the fluorescence lifetime decreases, the process is dynamic quenching.[42]

Here, after the addition of nitro-antibiotics, the fluorescence lifetime of the fluorophore was reduced from 1.68 ns to 1.28 and 1.38 ns for NFZ and NFT, respectively (Fig. S74, S75 and Tables S3, S4, ESI†). It confirmed the dynamic nature of quenching. Hence, the possibilities of IFE and static quenching are completely ruled out. For examination of the reason behind the quenching process in detail, we collected the UV-Vis spectra of all the antibiotics and the normalized absorption spectra were overlapped with the emission spectrum of **IITG-5a**. From Fig. S76,† it is obvious that the maximum overlap took place between the absorption spectra of nitro-antibiotics and the emission spectra of **IITG-5a**, whereas, all the other antibiotics did not show any overlap. This satisfactory overlap resulted in the resonance energy transfer from **IITG-5a** to the nitro-antibiotics. This is the possible reason behind quenching in fluorescence intensity, which was further supported by the decrease in fluorescence lifetime value. It is worthily to note that the above-discussed mechanism was followed in many of the sensing processes of nitro-antibiotics reported in the literature.[30,47,51]

Some fluorescence control experiments were also carried out using linkers **L1** and **L2** to confirm the energy transfer mechanism behind the sensing of NFT/NFZ in MeOH. Quenching in fluorescence emission maxima of the free linkers was observed for both the linker molecules after addition of 100 μL of 10 mM methanolic solutions of NFT/NFZ to the solution of the linkers (Fig. S77 and S78, ESI†). To explore these observations, we plotted the previously collected UV-Vis absorption spectra of all the antibiotics with the normalized emission spectra of the free linkers. Fig. S79 (ESI†) clearly displays the significant overlap between the emission spectrum of the linkers and the absorption spectra of the NFT/NFZ. These observations clearly support the energy transfer between the electron-rich donor linkers to electron-deficient nitro-antibiotics (NFZ and NFT). Such energy transfer is also possible for **L2** linker molecules. All the above-mentioned facts proved that the energy transfer process is the reason behind the sensing of NFT/NFZ by the MOF **IITG-5a** in a MeOH medium.

For the confirmation of the photo-induced electron transfer (PET) between the electron-rich donor MOF to electron-deficient nitro-antibiotics (NFZ and NFT), we executed the DFT calculations using the Gaussian 09 software. The functional, B3LYP and Pople diffuse basis set 6-31G were utilized for all

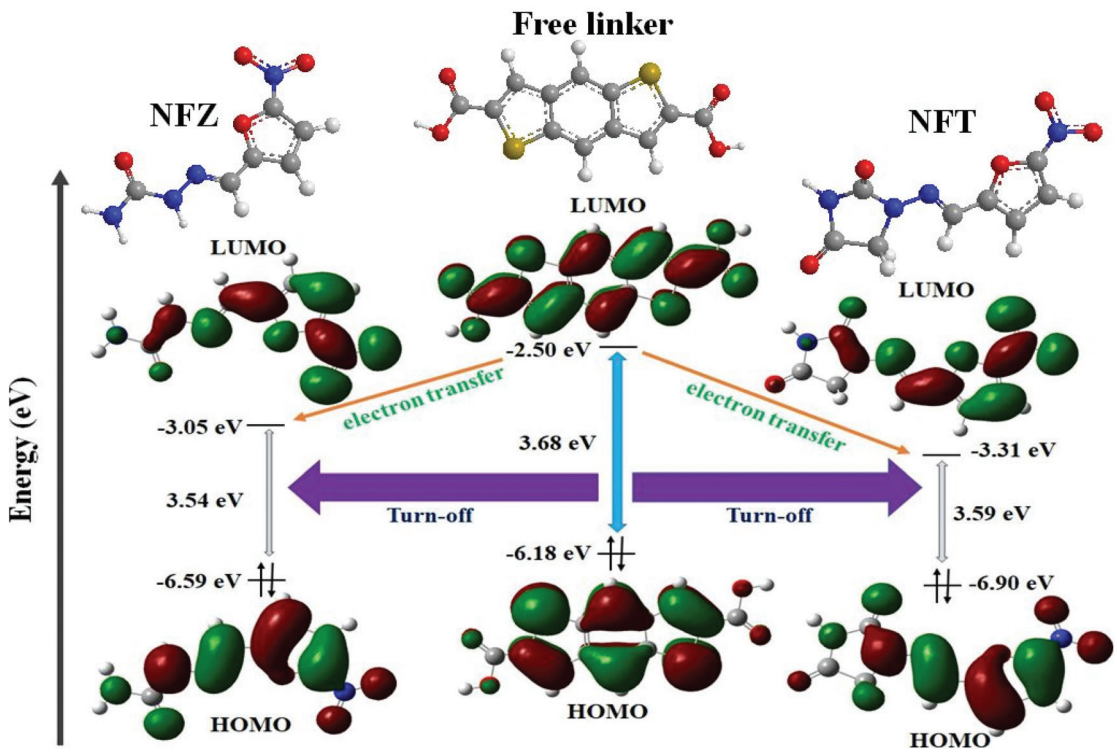

Fig. 9 HOMO–LUMO energy levels of the linker, NFZ and NFT obtained from the DFT calculations using the Gaussian 09 software.

the calculations. The aim of these calculations was to know the exact location of the HOMOs and LUMOs of the linker molecule and the targeted sensing analytes. For an ideal electron transfer process, the LUMOs of the electron-lacking analytes should stay in a lower energy level than the conduction band of the electron-rich probes. After DFT calculation with the linker molecule and nitro-antibiotics, we observed that the energy of the LUMO of the linker (−2.50 eV) is higher than the LUMO of the nitro-antibiotics (NFZ: −3.05 and NFT: −3.31 eV) (Fig. 9 and ESI†). Such alignment of energy levels facilitated the PET process. These theoretical observations were also supported by the UV-Vis spectroscopic observations.

Sensing of Hg^{2+} and nitro-antibiotics in paper strips

In recent times, the use of sensor-coated, cheap paper strips has rapidly increased for the in-field monitoring of toxic analytes. Here, we also verified the ability of our newly synthesized **IITG-5a** to sense our targeted analytes in a paper strip coated with **IITG-5a**. For this experiment, two filter paper strips were taken and both of them were homogeneously coated with **IITG-5a**. Then, **IITG-5a**-coated paper strips were dried and treated with a Hg^{2+} solution. After treating with Hg^{2+}, both of the filter papers were placed under UV-light. A strong blue fluorescence was observed in case of the un-treated paper strip but no fluorescence was observed for the Hg^{2+}-treated paper strip (Fig. S80, ESI†). This result implies that **IITG-5a** can sense Hg^{2+} in a paper strip. Analogous experiments were carried out in case of both the nitro-antibiotics and similar observations were obtained in case of both the antibiotics (Fig. S81, ESI†). Therefore, it can be concluded that real-time monitoring of Hg^{2+} and nitro-antibiotics is possible using **IITG-5a**-coated paper strips.

Conclusions

A Zr(IV)-metal-based UiO-66 type MOF has been successfully synthesized using a benzo[1,2-*b*:4,5-*b*′]dithiophene-2,6-dicarboxylic acid linker molecule. After single-step solvothermal synthesis, the material was throughout characterized using various instrumental supports (PXRD, elemental analysis, EDX, FE-SEM and IR analysis). Both **IITG-5** and **IITG-5a** displayed outstanding thermal stability up to a temperature of 390 °C. Excellent chemical stability of this porous material (surface area = 1228 $m^2\ g^{-1}$) in various solvents (H_2O, MeOH, CH_2Cl_2, acetone, hexane and DMF) was observed. The thermally activated compound showed the super selective nature of sensing towards Hg^{2+} in H_2O, and NFZ and NFT in a MeOH medium. Along with fast response (1 min for all analytes), nanomolar level detection capability (LOD: Hg^{2+} = 5 nM, NFZ = 156.7 nM and NFT = 96.3 nM) was observed in all the cases of sensing. A real-time paper strip method of sensing technique was also developed for all the sensing targets. In-depth investigations were carried out to establish the mechanisms for all the cases of sensing by analytical and spectroscopic methods as well as molecular simulations.

Author contributions

All the authors contributed to write this manuscript and the final version of this manuscript is submitted according to the approval of all the authors.

Conflicts of interest

There are no conflicts to declare.

Acknowledgements

We acknowledge funding from SERB (India) *via* the grant number EEQ/2016/000012.

Notes and references

1 B. L. Rivas, S. Villegas, B. Ruf and I. M. Peric, Removal of Metal Ions with Impact on the Environment by Water-insoluble Functional Copolymers: Synthesis and Metal ion Uptake Properties, *J. Chil. Chem. Soc.*, 2007, **52**, 1164–1168.
2 M. o. t. E. Environmental Health Department, *Minimata Disease: The History and Measures*, Ministry of the Environment, Government of Japan, Tokyo, Japan, 2002.
3 F. Ma, M. Sun, C. Yuan, J. Yao and S. Wang, A Novel Fluorescent Sensor for the Sensitive Detection of Mercury, *APCBEE Proc.*, 2014, **10**, 12–15.
4 C. C. Bridges, B. F. Krasnikov, L. Joshee, J. T. Pinto, A. Hallen, J. Li, R. K. Zalups and A. J. L. Cooperb, New Insights into the Metabolism of Organomercury Compounds: Mercury-containing Cysteine S-conjugates are Substrates of Human Glutamine Transaminase K and Potent Inactivators of Cystathionine γ-lyase, *Arch. Biochem. Biophys.*, 2012, **517**, 20–29.
5 T. Rush, X. Liu and D. Lobner, Synergistic Toxicity of the Environmental Neurotoxins Methylmercury and β-N-methylamino-L-alanine, *NeuroReport*, 2012, **23**, 216–219.
6 R. K. B. Barvin, P. Prakash, V. Ganesh and B. Jeyaprabha, Highly Selective and Sensitive Sensing of Toxic Mercury Ions Utilizing Carbon Quantum Dot-Modifed Glassy Carbon Electrode, *Int. J. Environ. Res. Public Health*, 2019, **13**, 1015–1023.
7 C. T. Driscoll, R. P. Mason, H. M. Chan, D. J. Jacob and N. Pirrone, Mercury as a Global Pollutant: Sources, Pathways, and Effects, *Environ. Sci. Technol.*, 2013, **47**, 4967–4983.
8 S. Flasche and K. E. Atkins, Balancing Benefits and Risks of Antibiotic Use, *J. Infect. Dis.*, 2018, **218**, 1351–1353.
9 R. Gaynes, The Discovery of Penicillin—New Insights After More Than 75 Years of Clinical Use, *Emerging Infect. Dis.*, 2017, **5**, 849–853.
10 T. P. V. Boeckel, S. Gandra, A. Ashok, Q. Caudron, B. T. Grenfell, S. A. Levin and R. Laxminarayan, Global Antibiotic Consumption 2000 to 2010: An Analysis of

National Pharmaceutical Sales Data, *Lancet Infect. Dis.*, 2014, **14**, 742–750.
11 B. Sloan and N. Scheinfeld, The Use and Safety of Doxycycline Hyclate and Other Second-generation Tetracyclines, *Expert Opin. Drug Saf.*, 2008, **7**, 571–577.
12 A. K. Mittal, R. Bhardwaj, P. Mishra and S. K. Rajput, Antimicrobials Misuse/Overuse: Adverse Effect, Mechanism, Challenges and Strategies to Combat Resistance, *Biotechnol. J.*, 2020, **14**, 107–112.
13 C. Llor and L. Bjerrum, Antimicrobial Resistance: Risk Associated with Antibiotic Overuse and Initiatives to Reduce the Problem, *Ther. Adv. Drug Saf.*, 2014, **5**, 229–241.
14 A. B. A. Boxall, D. W. Kolpin, B. Halling-Sørensen and J. Tolls, Are veterinary medicines causing environmental risks?, *Environ. Sci. Technol.*, 2003, **37**, 286–294.
15 O. O. Komolafe, Antibiotic Resistance in Bacteria-An Emerging Public Health Problem, *Malawi Med. J.*, 2003, **15**, 63–67.
16 B. J. Gardiner, A. J. Stewardson, I. J. Abbott and A. Y. Peleg, Nitrofurantoin and Fosfomycin for Resistant Urinary Tract Infections: Old Drugs for Emerging Problems, *Aust. Prescr.*, 2019, **42**, 14–19.
17 A. Ryan, E. Kapla, N. Laurieri, E. Lowe and E. Sim, Activation of Nitrofurazone by Azoreductases: Multiple Activities in One Enzyme, *Sci. Rep.*, 2011, **63**, 1–5.
18 L. L. Rego, C. S. Glazer and P. E. Zimmern, Risks of Long-term Use of Nitrofurantoin for Urinary Tract Prophylaxis in the Older Patient, *Urol. Sci.*, 2016, **27**, 193–198.
19 S. G. Bilgili, G. O. Yavuz, I. H. Yavuz, M. A. Bilgili and A. S. Karadag, Cutaneous Reactions Caused by Nitrofurazone, *Postepy Dermatol. Alergol.*, 2019, **36**, 398–402.
20 Y.-H. Shin, M. T. G. Wing and J.-W. Choi, Review—Recent Progress in Portable Fluorescence Sensors, *J. Electrochem. Soc.*, 2021, **168**, 017502.
21 N. Kwon, Y. Hu and J. Yoon, Fluorescent Chemosensors for Various Analytes Including Reactive Oxygen Species, Biothiol, Metal Ions, and Toxic Gases, *ACS Omega*, 2018, **3**, 13731–13751.
22 C. Gogoi, A. Kumar and M. SK, Specific Fluorescence Sensing of Hydrogen Sulphide by an Azide Functionalized Zr(IV) MOF with DUT-52 Topology, *Microporous Mesoporous Mater.*, 2021, **311**, 110725–110732.
23 S. Nandi and S. Biswas, Acetoxy Functionalized Al(III) Based Metal-organic Framework Showing Selective Turn on Detection of Perborate in Environmental Samples, *Dalton Trans.*, 2020, **49**, 17612–17620.
24 R. Dalapati, S. Nandi and S. Biswas, Post-Synthetic Modification of a Metal-Organic Framework with Chemodosimeter for Rapid Detection of Lethal Cyanide via Dual Emission, *Dalton Trans.*, 2020, **49**, 8684–8692.
25 V. Trannoy, N. Guillou, C. Livage, C. R. Marchal, M. Haouas, A. Leaustic, C. Allain, G. Clavier, P. Yu and T. Devic, Fluorescent Zr(IV) Metal–Organic Frameworks Based on an Excited-State Intramolecular Proton Transfer-Type Ligand, *Inorg. Chem.*, 2019, **58**, 6918–6926.
26 S. Nandi and S. Biswas, A Diamino Functionalized Metal-organic Framework for Fluorometric Recognition of Free Chlorine in Environmental Water Samples, *Microporous Mesoporous Mater.*, 2020, **299**, 110116–110124.
27 R. Dalapati and S. Biswas, Aqueous Phase Sensing of Fe^{3+} and Ascorbic Acid by a Metal–Organic Framework and Its Implication in the Construction of Multiple Logic Gates, *Chem. – Asian J.*, 2019, **14**, 2822–2830.
28 M. Ponram, U. Balijapalli, B. Sambath, S. K. Iyer, B. Venkatachalapathy, R. Cingarama and K. N. Sundaramurthy, Development of Paper-based Chemosensor for the Detection of Mercury Ions Using mono- and tetra-sulfur Bearing Phenanthridines, *New J. Chem.*, 2018, **42**, 8530–8536.
29 J.-M. Li, R. Li and X. Li, Construction of Metal–organic Frameworks (MOFs) and Highly Luminescent EuIJ(III)-MOF for the Detection of Inorganic Ions and Antibiotics in Aqueous Medium, *CrystEngComm*, 2018, **20**, 4962–4972.
30 H. He, Q.-Q. Zhu, M.-T. Guo, Q.-S. Zhou, J. Chen, C.-P. Li and M. Du, Doubly Interpenetrated Zn_4O-Based Metal–Organic Framework for CO_2 Chemical Transformation and Antibiotic Sensing, *Cryst. Growth Des.*, 2019, **19**, 5228–5236.
31 J. H. Cavka, S. Jakobsen, U. Olsbye, N. Guillou, C. Lamberti, S. Bordiga and K. P. Lillerud, A New Zirconium Inorganic Building Brick Forming Metal Organic Frameworks with Exceptional Stability, *J. Am. Chem. Soc.*, 2008, **42**, 13850–13851.
32 *Accelrys Incorporated*, Materials Studios, San Diego, 2009.
33 A. A. Coelho, TOPAS and TOPAS-Academic: an optimization program integrating computer algebra and crystallographic objects written in C++, *J. Appl. Crystallogr.*, 2018, **51**, 210–218.
34 A. Das, N. Anbu, M. SK, A. Dhakshinamoorthy and S. Biswas, Influence of Hydrogen Bond Donating Sites in UiO-66 Metal-Organic Framework for Highly Regioselective Methanolysis of Epoxides, *ChemCatChem*, 2020, **12**, 1789–1798.
35 A. Das, N. Anbu, H. Reinsch, A. Dhakshinamoorthy and S. Biswas, A Thiophene-2-carboxamide-Functionalized Zr (IV) Organic Framework as a Prolific and Recyclable Heterogeneous Catalyst for Regioselective Ring Opening of Epoxides, *Inorg. Chem.*, 2019, **58**, 16581–16591.
36 R. Dalapati, S. Nandi, C. Gogoi, A. Shome and S. Biswas, Metal-Organic Framework (MOF) Derived Recyclable, Superhydrophobic Composite of Cotton Fabrics for the Facile Removal of Oil Spills, *ACS Appl. Mater. Interfaces*, 2021, **13**, 8563–8573.
37 D. Zou and D. Liu, Understanding the Modifications and Applications of Highly Stable Porous Frameworks via UiO-66, *Mater. Today Chem.*, 2019, **12**, 139–165.
38 Y. Kim, R. C. Johnson and J. T. Hupp, Gold Nanoparticle-Based Sensing of "Spectroscopically Silent" Heavy Metal Ions, *Nano Lett.*, 2001, **1**, 165–167.
39 S. Bayindir, A Simple Rhodanine-based Fluorescent Sensor for Mercury and Copper: The Recognition of Hg^{2+} in

Aqueous Solution, and Hg^{2+}/Cu^{2+} in Organic Solvent, *J. Photochem. Photobiol., A*, 2019, **372**, 235–244.

40 P. Wu, Y. Liu, Y. Liu, J. Wang, Y. Li, W. Liu and J. Wang, Cadmium-Based Metal–Organic Framework as a Highly Selective and Sensitive Ratiometric Luminescent Sensor for Mercury(II), *Inorg. Chem.*, 2015, **54**, 11046–11048.

41 Y. Zhao, X. Xu, L. Qiu, X. Kang, L. Wen and B. Zhang, Metal–Organic Frameworks Constructed from a New Thiophene-Functionalized Dicarboxylate: Luminescence Sensing and Pesticide Removal, *ACS Appl. Mater. Interfaces*, 2017, **9**, 15164–15175.

42 Y. Li, K. Liu, W.-J. Li, A. Guo, F.-Y. Zhao, H. Liu and W.-J. Ruan, Coordination Polymer Nanoarchitecture for Nitroaromatic Sensing by Static Quenching Mechanism, *J. Phys. Chem. C*, 2015, **119**, 28544–28550.

43 H. Sohn, M. J. Sailor, D. Magde and W. C. Trogler, Detection of Nitroaromatic Explosives Based on Photoluminescent Polymers Containing Metalloles, *J. Am. Chem. Soc.*, 2003, **125**, 3821–3830.

44 G. R. You, S. Y. Lee, J. J. Lee, Y. S. Kim and C. Kim, Sequential Detection of Mercury(II) and Thiol-containing Amino Acids by a Fluorescent Chemosensor, *RSC Adv.*, 2016, **6**, 4212–4220.

45 Q. Mei, Y. Shi, Q. Huaa and B. Tong, Phosphorescent Chemosensor for Hg^{2+} Based on an Iridium(III) Complex Coordinated with 4-phenylquinazoline and Carbazole Dithiocarbamate, *RSC Adv.*, 2015, **5**, 74924–77493.

46 A. Singh, S. Kaur, N. Singh and N. Kaur, Fluorometric Sensing of Hg^{2+} Ions in Aqueous Medium by Nano-aggregates of a Tripodal Receptor, *Org. Biomol. Chem.*, 2014, **12**, 2302–2309.

47 F. Zhang, H. Yao, T. Chu, G. Zhang, Y. Wang and Y. Yang, A Lanthanide MOF Thin-Film Fixed with Co3O4 Nano-Anchors as a Highly Efficient Luminescent Sensor for Nitrofuran Antibiotics, *Chem. – Eur. J.*, 2017, **23**, 10293–10300.

48 K. Xing, R. Fan, X. Du, X. Zheng, X. Zhou, S. Gai, P. Wang and Y. Yang, Dye-insertion Dynamic Breathing MOF as Dual-emission Platform for Antibiotics Detection and Logic Molecular Operation, *Sens. Actuators, B*, 2019, **288**, 307–315.

49 Q.-Q. Zhu, Q.-S. Zhou, H.-W. Zhang, W.-W. Zhang, D.-Q. Lu, M.-T. Guo, Y. Yuan, F. Sun and H. He, Design and Construction of a Metal–Organic Framework as an Efficient Luminescent Sensor for Detecting Antibiotics, *Inorg. Chem.*, 2020, **59**, 1323–1331.

50 S. Nandi, A. Mondal, H. Reinsch and S. Biswasa, An Ultra-robust Luminescent CAU-10 MOF Acting as a Fluorescent "Turn-off" Sensor for $Cr_2O_7^{2-}$ in Aqueous Medium, *Inorg. Chim. Acta*, 2019, **497**, 119078–119087.

51 H.-B. Zhu and Z.-Y. Sun, Aqueous Detection of Antibiotics with a Cd(II)-based Metal-organic Framework Constructed by a tetra(1,2,4-triazole)-Functionalized-bis (triphenylamine) Ligand, *Inorg. Chem. Commun.*, 2018, **96**, 202–205.